CHEMISTRY OF MATERIALS

pubs.acs.org/cm

Article

Enhanced Hardening Effects on Molybdenum-Doped WB_2 and WB_2−SiC/B_4C Composites

Lisa E. Pangilinan, Shanlin Hu, Christopher L. Turner, Jinyuan Yan, Abby Kavner, Reza Mohammadi, Sarah H. Tolbert,* and Richard B. Kaner*

Cite This: *Chem. Mater.* 2022, 34, 5461−5470

Read Online

ACCESS | Metrics & More | Article Recommendations | Supporting Information

ABSTRACT: Tungsten diboride (WB_2) solid solutions with increasing molybdenum (Mo) substitution were synthesized by resistive arc-melting from the pure elements and characterized for their mechanical properties. The WB_2-type structure is maintained up to 30 atomic percent (at%) Mo substitution. $W_{0.70}Mo_{0.30}B_2$ achieved a maximum Vickers hardness of 45.7 ± 2.5 GPa at 0.49 N, resulting in the hardest WB_2 solid solution to date. In agreement with this fact, high-pressure radial diffraction studies indicate that substitution of Mo into WB_2 strengthens metal−boron bonding, as the solid solution supports high differential stress and has a bulk modulus of 355 ± 2 GPa. WB_2 and $W_{0.70}Mo_{0.30}B_2$ composites were then synthesized with increasing additive content (0−30 wt%) of B_4C or SiC to study extrinsic hardening effects through multiphase formation. These composites show extrinsic effects on the Vickers hardness because of secondary-phase precipitation. While WB_2−30 wt% B_4C exhibited the highest hardness (53.8 ± 6.0 GPa at 0.49 N), WB_2−30 wt% SiC demonstrated the slowest oxidation rate. This work offers new insights for tailoring transition-metal boride systems with optimized hardness, grain morphology, and thermal stability.

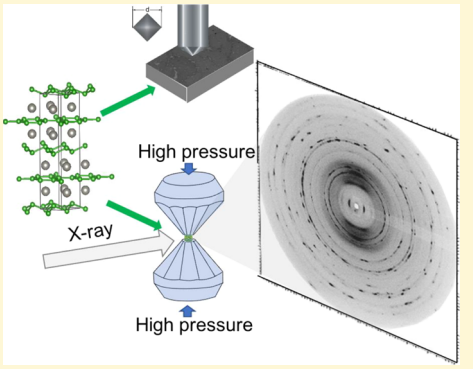

INTRODUCTION

The search for novel superhard materials is motivated by the demand for high-performance cutting tools and abrasives with enhanced mechanical properties and thermal stability.[1,2] While frequently reported at the high load asymptotic limit, superhardness (Vickers hardness, $H_v \geq 40$ GPa) is often observed at lower load (0.49 N), which is more compatible with real-world applications. Hardness values reported over a range of low and high loads can be utilized to understand the origin of hardness in the bulk material and to assess a material's utility at the applied loads required for various industrial cutting operations. Although diamond is the most commercially relevant superhard material, diamond's use is limited by its cost-prohibitive synthesis (requiring both high temperature and high pressure) as well as its high reactivity to ferrous alloys (resulting in poor cutting performance and poor stability above 700 °C).[3,4] These shortcomings have inspired the creation of new superhard materials that are readily synthesized, thermally stable, and made from less expensive elements.[5,6]

Because of their highly covalent bonding networks, several metal boride systems (e.g., ReB_2 and WB_4) have been identified as superhard at low load.[7,8] The intrinsic hardness of these materials can be further increased through the formation of solid solutions, where an alloying element with a valence electron count and/or size that is different from the parent metal is substituted into the host structure.[9] These solid solutions employ the Hume-Rothery rules, where the parent metal and dopant atoms need to: (1) be less than 15% different in atomic radius, (2) adopt similar crystal structures, (3) have similar electronegativity values, and (4) be close in valence electron density.[10−12] When atom mixtures fall outside of these bounds, two-phase coexistence generally occurs, preventing favorable solid solution hardening. Two-phase mixtures can, however, show increased hardness because of extrinsic effects and include grain boundary strengthening and precipitation hardening, where the reduction in the average grain size and precipitation of secondary phase(s) increase the degree of grain boundaries and dislocation pinning in the bulk material.[13,14]

Transition-metal diborides have been extensively studied for their superconductivity, electrocatalytic performance, and high hardness.[15−18] Most diborides, such as TiB_2 and ZrB_2, exhibit an AlB_2-type structure ($P6/mmm$), which contains flat boron sheets and 12-coordinate metal layers.[19,20] Such materials tend not to be terribly hard, because of easy slip parallel to the flat boron sheets. In the ReB_2 structure ($P6_3/mmc$), boron sheets adopt a corrugated, chair configuration that impedes slip plane

Received: February 6, 2022
Revised: May 26, 2022
Published: June 14, 2022

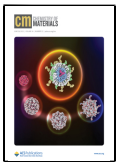

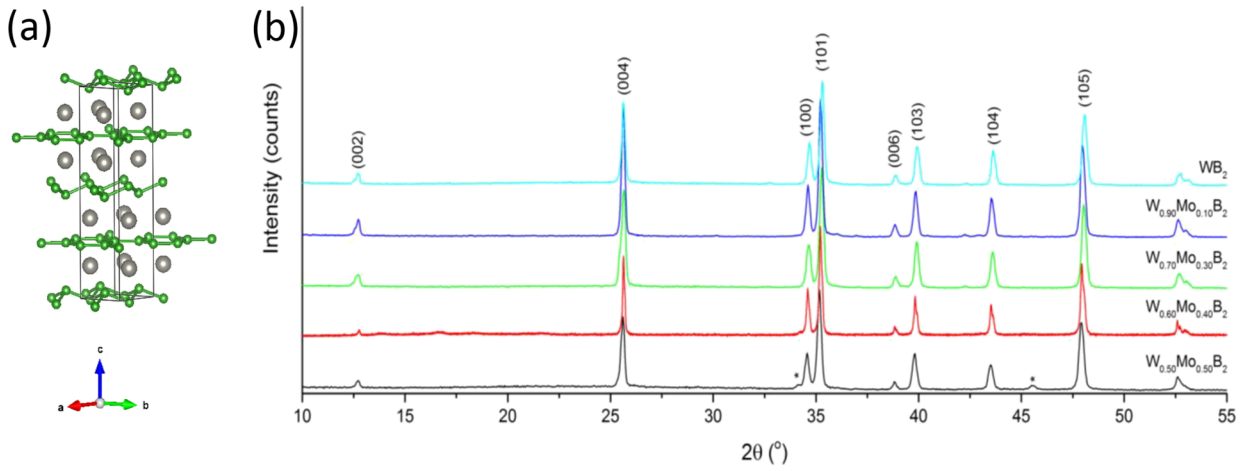

Figure 1. (a) Crystal structure of tungsten diboride, WB_2 [$P6_3/mmc$, Inorganic Crystal Structure Database (ICSD) 023716], where the unit cell is indicated by the black box. Boron atoms are represented in green as flat and puckered alternating sheets. Tungsten atoms are represented in gray. (b) Selected PXRD data of tungsten diboride (WB_2) solid solutions with up to 50 at% molybdenum (Mo). The solubility limit is below 40 at% Mo. WB_2 (JCPDS 00-043-1386) is present at all concentrations of Mo, while β-MoB_2 (JCPDS 01-075-1046) appears in the 40 and 50 at% Mo samples, denoted by an asterisk (*).

motion.[21,22] With a hybrid structure containing alternating flat and corrugated boron sheets between metal layers, tungsten diboride (WB_2, $P6_3/mmc$) is a candidate structure in the design of new superhard materials (Figure 1).[23,24] Although pure WB_2 is not intrinsically superhard, substitutional solid solutions of WB_2 have been characterized with hardness values measuring in the superhard regime.[25]

In addition to single-phase systems, many studies have examined the microstructure and properties of multiphase composites based on metal diborides.[26] For instance, secondary additives, such as boron carbide (B_4C) and/or silicon carbide (SiC), have been shown to decrease the grain size of metal diborides, such as ZrB_2 and TiB_2, in ultrahigh-temperature ceramics and enhance bulk mechanical properties.[27,28] Thus, it is of great interest to identify the contributions of both intrinsic and extrinsic hardening effects in order to optimize a material's grain morphology and mechanical properties.

In this study, we synthesize molybdenum (Mo)-doped WB_2 solid solutions and characterize their mechanical properties as a function of solubility. Given that Mo (1.45 Å)[29] has the same number of valence electrons (group 6) and a close atomic radius to W (1.35 Å),[29] we have obtained an extended range of solid solutions. The material is phase-pure at concentrations up to and including 30 at% Mo in WB_2, but higher Mo incorporation levels can be achieved in materials that contain small amounts of β-MoB_2 mixed with the $W_xMo_{1-x}B_2$. Vickers hardness measurements, high-pressure data, and scanning electron microscopy (SEM) images are discussed in further detail to demonstrate that the addition of Mo enhances bulk material hardness through both solid-solution formation and additional extrinsic affects through a change in surface morphology. Additionally, we study the effects of secondary phases, SiC and B_4C, on both unsubstituted WB_2 and 30 at% Mo-substituted WB_2 ($W_{0.70}Mo_{0.30}B_2$), the hardest WB_2 solid solution created to date. These two-phase composites show extrinsic hardening through the inhibition of grain growth and increased oxidation resistance through enhanced phase stability and protective oxide formation during thermal cycling.

EXPERIMENTAL PROCEDURE

Samples were prepared using tungsten (99.95%, Strem Chemicals, USA), amorphous boron (99 + %, Strem Chemicals, USA), molybdenum (99.95%, Strem Chemicals, USA), silicon (99.9%, American Elements, USA), and carbon (graphite, 99+%, Strem Chemicals, USA). Elemental boron and metal powders were weighed and mixed according to the following nominal compositions: $W_{1-x}Mo_xB_{2.0}$, where x = 0.02−0.50. Composites were prepared by weighing and mixing elemental powders according to the compositions: $WB_{2.0}$-B_4C, $WB_{2.0}$-SiC, $W_{0.70}Mo_{0.30}B_{2.0}$-B_4C, and $W_{0.70}Mo_{0.30}B_{2.0}$-SiC, where the weight percentage of B_4C or SiC in each total composition was varied (10, 20, and 30 wt%). The powder mixtures were pressed into 12.7 mm (0.5 in) diameter pellets under a 10-ton load using a hydraulic jack press (Carver, USA). The pressed pellets were arc-melted on a water-cooled copper hearth in an argon atmosphere with a maximum current of approximately 140 amps for 1−2 min. Each sample was arc-melted until molten, subsequently flipped, and remelted, totaling three times to ensure homogeneity.

The sample ingots were bissected using a diamond saw (Ameritool Inc., USA). One half of each sample was crushed into <45 μm powder (−325 mesh) for powder X-ray diffraction analysis (PXRD) and thermogravimetric analysis (TGA) using a tool steel Plattner-style mortar and pestle set (Humboldt Mfg., model H-17270). The other half was cold-mounted in epoxy using an epoxy/hardener set (Buehler, USA) and polished on a semiautomated polishing station (Buehler, USA). To produce an optically flat surface, each sample was polished with silicon carbide disks (120−600 grit sizes, Buehler, USA) followed by polishing cloths independently coated in polycrystalline diamond suspensions with particle sizes ranging from 15 to 0.25 μm (Buehler, USA). Polished samples were used for SEM, energy-dispersive spectroscopy (EDS), and Vickers hardness testing.

PXRD was performed on a Bruker D8 Discover Powder X-ray Diffractometer (Bruker Corporation, Germany) to determine the composition and phase purity of the crushed powder samples. Data were acquired using a $Cu_{K\alpha}$ X-ray beam (λ = 1.5418 Å) in the 5−100° 2θ range. PXRD data were compared with the International Centre for Diffraction Data (ICDD) patterns, formerly known as the Joint Committee on Powder Diffraction Standards (JCPDS), in order to identify the phases present in each sample. Unit cell refinements were performed using GSAS-II.[30] An FEI Nova 230 high-resolution scanning electron microscope (FEI Company, USA) equipped with a backscattered electron detector (BSED) and an UltraDry EDS detector (Thermo Scientific, USA) was used to analyze the surface morphology and elemental composition of the polished samples.

https://doi.org/10.1021/acs.chemmater.2c00386
Chem. Mater. 2022, 34, 5461−5470

Vickers hardness measurements were performed using a multi-Vickers hardness tester (Leco, USA) with a pyramidal diamond indenter. Indentations were made on polished samples with applied force loads of 0.49, 0.98, 1.96, 2.94, and 4.9 N. The lengths of the diagonals of each indent were measured under 500x magnification using a high-resolution optical microscope, Zeiss Axiotech 100HD (Carl Zeiss Vision GmbH, Germany). Vickers hardness values (H_v in GPa) were calculated and averaged for 10 indents per load using the following formula (eq 1):

$$H_v = \frac{1854.4F}{d^2} \tag{1}$$

where F is the applied load (in Newtons) and d is the average length of the diagonals for an indent (in micrometers). A minimum of 10 indentations were performed in pseudorandom locations throughout the polished sample surface. Hardness values were reported at loads ranging from 0.49 to 4.9 N (low to high) in order to gain insight into the origin and load-dependency of a material's hardness.

A Pyris Diamond TGA/DTA unit (TG-DTA, PerkinElmer Instruments, USA) was used to study thermal stability (up to 1000 °C in standard nonmedical compressed air) under the following parameters: heat in air from 25 to 200 °C at a rate of 20 °C/min, hold at 200 °C for 30 min, heat from 200 to 1000 °C at 2 °C/min, hold at 1000 °C for 2 h, and cool from 1000 to 25 °C at 5 °C/min. PXRD was used to identify the resulting phase(s) of the heated samples.

Nonhydrostatic in situ high-pressure radial X-ray diffraction was performed in a diamond anvil cell at the synchrotron beamline 12.2.2 of the Advanced Light Source (ALS, Lawrence Berkeley National Laboratory). Crushed powder of the sample ($W_{0.70}Mo_{0.30}B_2$) was loaded into a laser-drilled hole (~60 μm in diameter, ~60 μm in depth) in an ~400 μm diameter boron gasket made of amorphous boron and epoxy. A small piece of Pt foil (~20 μm diameter) was placed on top of the sample to serve as an internal pressure standard. A monochromatic X-ray beam (λ = 0.4959 Å, spot size = 20 μm × 20 μm) was passed through the sample, which was compressed between two diamond tips up to 60 GPa of pressure, and two-dimensional (2-D) diffraction data were collected using an MAR-345 image plate and FIT2D software. A cerium dioxide (CeO_2) standard was used to calibrate the detector distance and orientation. The angle-dispersive diffraction patterns were converted from elliptical to rectangular coordinates using FIT2D. The integrated "cake" patterns, azimuthal angle (η) versus diffraction angles (2θ), were then analyzed using Igor Pro (WaveMetrics, Inc.). Peak positions were manually picked for three easily resolvable diffraction peaks (004, 101, and 110). The one-dimensional diffractions of X-ray intensity as a function of 2θ were obtained at the magic angle (φ = 54.7°, effectively hydrostatic condition). All peaks were indexed to hexagonal phases with no indication of phase transition throughout the measured pressure range.

The stress in the sample under uniaxial compression is described by eq 2:

$$\sigma = \begin{bmatrix} \sigma_1 & 0 & 0 \\ 0 & \sigma_1 & 0 \\ 0 & 0 & \sigma_3 \end{bmatrix} = \begin{bmatrix} \sigma_p & 0 & 0 \\ 0 & \sigma_p & 0 \\ 0 & 0 & \sigma_p \end{bmatrix} + \begin{bmatrix} -t/3 & 0 & 0 \\ 0 & -t/3 & 0 \\ 0 & 0 & -2t/3 \end{bmatrix} \tag{2}$$

where σ_1 is the minimum stress along the radial direction, σ_3 is the maximum stress in the axial direction, σ_P is the hydrostatic stress component, and t is the differential stress, which gives a lower-bound estimate of yield strength. The d-spacing is calculated by:

$$d_m(hkl) = d_p(hkl)[1 + (1 - 3\cos^2\varphi)Q(hkl)] \tag{3}$$

where d_m is the measured d-spacing, d_p is the d-spacing at hydrostatic peak position, φ is the angle between the diffraction normal and axial directions, and $Q(hkl)$ is the lattice strain under the uniaxial stress condition. The differential stress, t, is directly related to the differential strain, $t(hkl)/G(hkl)$, by:

$$t(hkl) = 6G(hkl)Q(hkl) \tag{4}$$

where $G(hkl)$ is the shear modulus of the specific lattice plane.

Incompressibility can be determined using the third-order Birch–Murnaghan equation-of-state (EOS), which is written as:

$$P = \frac{3}{2}K_0\left[\left(\frac{V_0}{V}\right)^{7/3} - \left(\frac{V_0}{V}\right)^{5/3}\right]\left[1 + \frac{3}{4}(K_0' - 4)\left[\left(\frac{V_0}{V}\right)^{2/3} - 1\right]\right] \tag{5}$$

where P is the pressure, K_0 is the bulk modulus at ambient pressure, V is the volume, V_0 is the undeformed unit cell volume, and K_0' is the derivative of K_0 with respect to P. Eq 5 can be simplified to second-order by fixing K_0' = 4. The Birch–Murnaghan EOS can also be rewritten in terms of normalized pressure (F) and Eulerian strain (f), as shown in the following:

$$F = \frac{P}{3f(1 + 2f)^{5/2}} \tag{6}$$

$$f = \frac{1}{2}\left[\left(\frac{V_0}{V}\right)^{2/3} - 1\right] \tag{7}$$

Eqs 6 and 7 can be combined to give a linear regression, where the zero-intercept yields the bulk modulus at ambient pressure (K_0) and the slope gives the pressure derivatives of the bulk modulus (K_0').

RESULTS AND DISCUSSION

Intrinsic Properties of Mo-Doped WB_2. Here, we investigate the effects of molybdenum substitution on WB_2 solid solutions ($W_{1-x}Mo_xB_2$). For a structure to be a solid solution, it must exhibit a linear change in the unit cell volume with increasing solute concentration. The concentration of atomic substitution (at% of solute), before the secondary-phase precipitation appears indicates the substitution threshold, or solubility limit, for that particular solute. Figure 1 shows PXRD patterns for $W_{1-x}Mo_xB_2$, where the solubility limit of Mo in WB_2 is below 40 at% Mo. Rietveld refinement was performed using GSAS-II software to calculate the unit cell parameters of Mo-substituted solid solutions through comparison with the WB_2 structure ($P6_3/mmc$). The c/a axial ratio and unit cell volume for the WB_2–Mo system from 0–50 at% Mo addition are presented in Figure 2. As the percentage of Mo increases, the c/a ratio decreases while the overall volume increases. These results indicate a higher rate of unit cell expansion along the a-axis with increasing Mo substitution. The observed lattice expansion is in adherence with Vegard's law and substitutional solid solution formation as Mo substitutes for W in W sites in the WB_2 lattice across all concentrations, despite the appearance of a small amount of β-MoB_2 in the higher Mo samples.

The systematic shift in the WB_2 peaks across all 2θ values and the collective change in the c/a ratio, shown in Figures 1 and 2, respectively, indicate the formation of solid solutions. Moreover, the refined diffraction patterns in Figure S1 indicate that no MoB_2 (R-3m) is present at or below 30% Mo doping. Some additional peaks do appear in the diffraction patterns at lower Mo concentrations; however, the fact that the impurity peaks appear at the same positions in all samples, including the pure WB_2 sample, indicates that the impurity is not a Mo-containing phase. Indeed, the peak positions are in good agreement with the WB diffraction pattern, and the relative intensity of the WB peaks to WB_2 peaks suggests that the samples contain less than 5 wt% of the WB phase.

https://doi.org/10.1021/acs.chemmater.2c00386
Chem. Mater. 2022, 34, 5461–5470

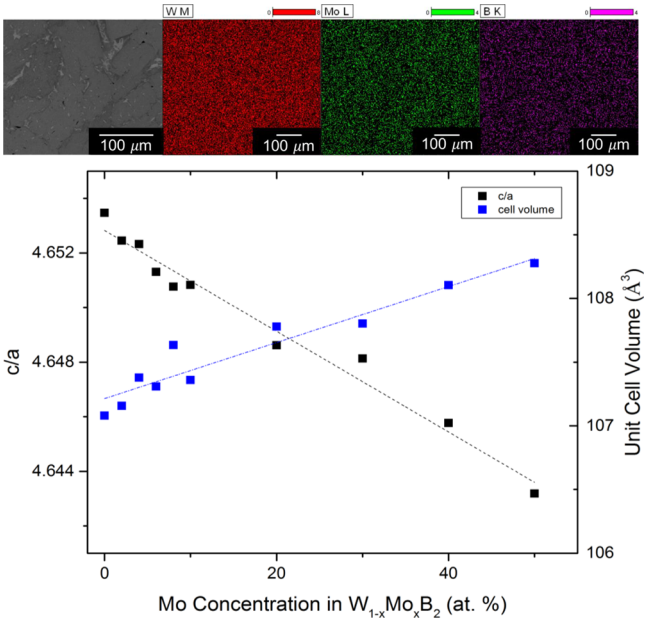

Figure 2. (Top) SEM BSED image and elemental maps for tungsten (M line), molybdenum (L line), and boron (K line) for $W_{0.70}Mo_{0.30}B_2$ showing a uniform distribution of tungsten and molybdenum throughout the grains. (Bottom) Plot of (black) axial ratio, c/a, calculated from XRD cell refinement and (blue) unit cell volume calculated from $W_{1-x}Mo_xB_2$ lattice parameters versus Mo concentration in atomic percentage. Dashed lines represent linear trendlines as a function of Mo concentration. Unit cell parameters of all compositions are provided in Table S1.

SEM images and elemental maps of $W_{0.70}Mo_{0.30}B_2$, the composition of maximum Mo solubility, show an even distribution of Mo up to 30 at% substitution and indicate no secondary-phase formation (Figure 2). Above the solubility limit, a secondary phase, β-MoB_2 ($P6/mmm$), precipitates upon cooling from the melt. While XRD analysis demonstrates the presence of MoB_2 precipitates above 30 at% Mo (Figure 1), the WB_2 lattice still continues to expand linearly with 40 and 50 at% Mo substitution (Figure 2). This volume expansion past the solubility limit suggests that many of the Mo atoms may still further substitute into the WB_2 structure in addition to forming a secondary MoB_2 phase.

Vickers microindentation hardness measurements from low to high load (0.49 to 4.9 N) for the WB_2−Mo system are shown in Figure 3. All solid solutions exhibit load-dependent hardness values, where the hardness increases as the applied load decreases. This phenomenon, known as the indentation size effect, has been observed in the hardness of other systems and is likely due to the fact that more slip systems become accessible at higher load.[31] A gradual increase in hardness was observed from 29.5 ± 1.7 GPa at 0.49 N for unsubstituted WB_2 to a maximum value of 45.7 ± 2.5 GPa at 0.49 N with 30 at% Mo. Above 30 at% Mo, the hardness abruptly decreases because of the precipitation of the softer AlB_2-type β-MoB_2 phase (11.77 GPa at 0.49 N).[32]

Unlike ReB_2, which adopts a puckered boron structure that impedes dislocation slip, WB_2 contains alternating flat and puckered boron sheets, resulting in lower shear resistance than ReB_2. In situ X-ray radial diffraction was conducted under nonhydrostatic compression up to 60 GPa to probe changes in bond length and strength within $W_{0.70}Mo_{0.30}B_2$ upon pressure. The "cake" patterns recorded at the lowest and highest

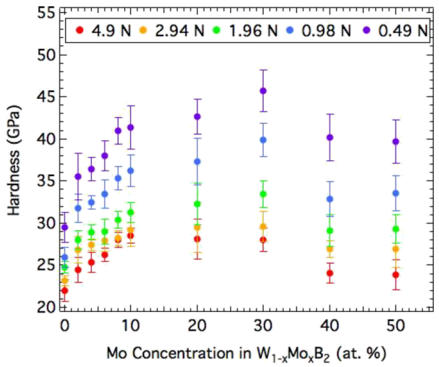

Figure 3. Vickers microindentation hardness versus atomic percentage of Mo in WB_2-Mo solid solutions from low (0.49 N) to high (4.9 N) load. Concentrations of Mo were varied by increasing the substitution of Mo from 0−50 at% on a metals basis.

pressures (3 and 60 GPa, respectively) and the integrated 1-dimensional diffraction patterns are shown in Figure 4. At low pressure (~3 GPa), the diffraction lines are almost straight because of the hydrostatic stress state. However, at high pressure, the diffraction lines deviate to a higher angle (2θ) in the high-stress direction ($\varphi = 0°$) and to a lower angle (2θ) in the low-stress direction ($\varphi = 90°$). The sinusoidal variations of the diffraction lines at high pressure indicate the lattice-supported strains (Figure 4b). In the integrated one-dimensional diffraction pattern obtained at the magic angle φ = 54.7°, all peaks can be indexed to the WB_2 structure throughout the measured pressure range (Figure 4a). A clear shift to the higher angle is observed at the higher pressure, indicating a decrease in the lattice spacing with greater compression. The peak broadening is due to strain inhomogeneity. The peak positions at φ = 54.7° are used to determine the lattice parameters and volume, as summarized in Table S2 and Figure S2. The pressure for each compression step was determined from the EOS of Au standard, using its d-spacing at φ = 54.7°.

As shown in Figure 5a, in the pressure range between 10 and 15 GPa, the c/a ratio undergoes a dramatic expansion, much larger in magnitude than the contraction that occurs upon Mo substitution (Figure 2). This sharp change in the c/a ratio is indicative of a pressure-induced second-order phase transition. Such transitions have not been observed in other layered diborides that we have studied, such as ReB_2,[33] but they have been observed in more structurally constrained metal borides that contain boron cages crosslinking the layers, such as WB_4 and its solid solutions.[34,35] Past studies have associated such pressure-induced changes in the c/a ratio with rigid structures that also tend to show high hardness. In addition to providing a probe of phase behavior, the hydrostatic compression curve is fit to extract the bulk modulus or volume incompressibility. Because of the low phase transition pressure and the small number of points below the phase transition, the data can only be fit in the high-pressure phase, at pressures above 15 GPa. A fit of volume change to the second-order Birch−Murnaghan EOS is shown in Figure S2c, and a normalized pressure versus Eulerian strain plot is shown in Figure 5b, yielding a bulk modulus of 355 ± 2 GPa ($K_0' = 4$) and 368.5 ± 3.6 GPa ($K_0' = 3.2$) for second-order and third-order Birch−Murnaghan EOSs, respectively.

To calculate the differential strain and stress, the measured d-spacing is plotted versus the orientation function (1−

https://doi.org/10.1021/acs.chemmater.2c00386
Chem. Mater. 2022, 34, 5461−5470

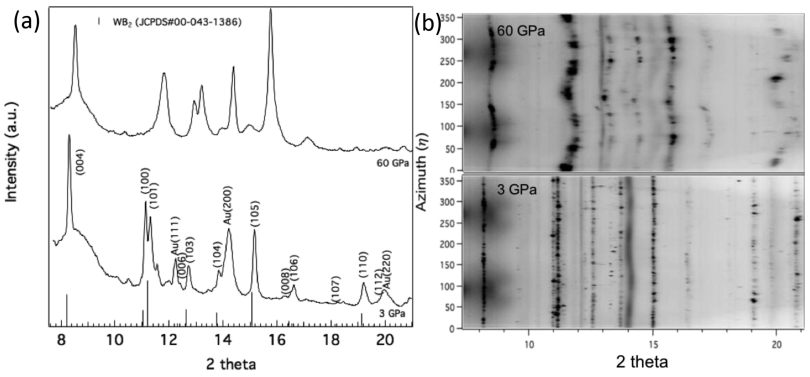

Figure 4. Representative synchrotron (a) 1-D X-ray diffraction patterns and (b) 2-D cake pattern of $W_{0.70}Mo_{0.30}B_2$ for low and high pressures. Cake patterns were obtained by integration over a 5° slice centered at the magic angle (φ = 54.7°).

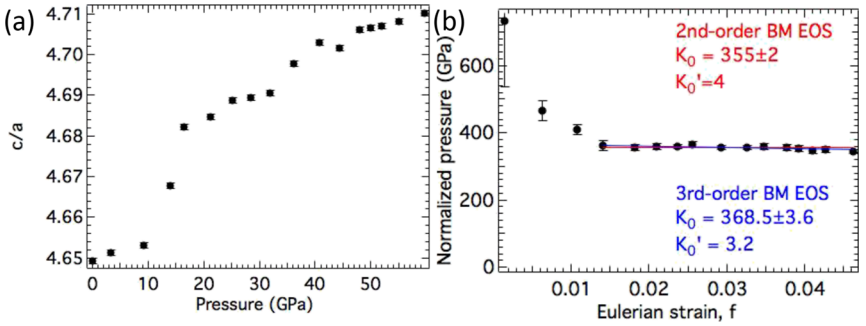

Figure 5. (a) Evolution of c/a upon pressure for $W_{0.70}Mo_{0.30}B_2$ obtained at the magic angle. (b) Normalized pressure (F) as a function of Eulerian strain (f). Second-order (red) and third-order (blue) Birch–Murnaghan EOS fits.

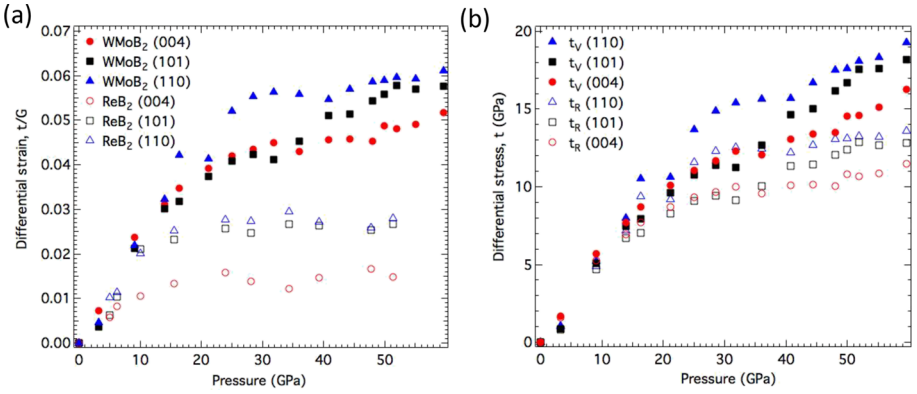

Figure 6. (a) Comparison of the differential strain, given by the ratio of the differential stress (t) to shear modulus (G), as a function of pressure for both $W_{0.70}Mo_{0.30}B_2$ ($WMoB_2$) and ReB_2. (b) Differential stress (t) calculated under Reuss (isostress, t_R) and Voigt (isostrain, t_V) conditions for $WMoB_2$.

$3\cos^2\varphi$) for each lattice plane of interest; a linear correlation is observed for the highest pressures, as shown in Figure S3 and in good agreement with lattice strain theory (eq 3). The hydrostatic d-spacings, obtained from zero-intercepts of linear fits like those shown in Figure S2, are found to shift smoothly with pressure, as shown in Figure S4. The ratio of the slope of the line in Figure S3 to the zero-intercept is directly related to the differential strain, $Q(hkl)$, as given by Eq 3. As shown in Figure 6, the measured differential strain for each lattice plane, presented here as t/G according to Eq 4, increases linearly with pressure and then appears to level off. The linear increase is associated with elastic behavior, including the second-order phase transition, and the plateau is interpreted to imply that the lattice plane can no longer sustain additional differential strain and presumably indicates the onset of plastic deformation (which is not clearly identifiable in the X-ray diffraction measurements). The plane with the lowest differential strain plateau value supports the least deformation, while planes with higher differential strain plateau values resist more shear and dislocation movement. The (004) plane, parallel to the boron layers, is prone to slip and therefore exhibits the lowest differential strain, particularly at the highest pressures. The (101) and (110) planes, both of which cut through the metal–boron layers, support more lattice deformation (Figure 6a). Interestingly, at lower pressures, $t(101)/G$ tracks almost perfectly with $t(004)/G$. However, part way through the (004) plateau, $t(101)/G$ deviates from $t(004)/G$ and eventually reaches a second plateau with the

https://doi.org/10.1021/acs.chemmater.2c00386
Chem. Mater. 2022, 34, 5461–5470

same value as $t(110)/G$ at 60 GPa. Data for the hardest pure metal diboride, ReB_2, are included for comparison. ReB_2 generally supports much lower differential strain and specifically shows a much lower plateau value for the (004) plane. ReB_2 also does not show strain hardening in the (101) plane. Together, these factors combine to indicate that substituting Mo into WB_2 may strengthen the metal−boron bonds in $W_{0.70}Mo_{0.30}B_2$.

The differential stress (t) value at the plateau indicates the yield strength of the plane upon shear and is directly correlated with hardness. Unfortunately, the appropriate choice of a shear modulus, G, requires knowledge of the stress state in the sample chamber during measurement. The differential stress can be calculated under Reuss (isostress) and Voigt (isostrain) conditions using the elastic stiffness constants provided in the paper by Ding et al.[36] Because the real differential stress is likely a weighted average of the Reuss and Voigt conditions, both values were calculated as upper and lower limits of the true differential stress. The differential stress of the (110) plane plateaus at 19 and 14 GPa under Voigt and Reuss conditions, respectively, suggests that the plane has reached its yield strength at the pressure achieved in this experiment (Figure 6b). The plateau in differential stress supported by (004), the weakest plane, reaches 11−16 GPa, which is higher than the strongest plane in ReB_2 (9−10 GPa).[33] The strain hardening the (101) plane is also preserved under both Reuss and Voight conditions. Although $W_{0.70}Mo_{0.30}B_2$ adopts the WB_2 structure, which deforms more readily than ReB_2, the presence of Mo dopant atoms in WB_2 apparently strengthens the covalent bonds and enables $W_{0.70}Mo_{0.30}B_2$ to support higher differential stress. These results indicate that increased hardness upon 30 at% Mo substitution in WB_2 is largely the result of intrinsic solid-solution strengthening in the single-phase system.

Previous calculations have predicted that the WB_2-type MoB_2 (WB_2−MoB_2, $P6_3/mmc$) is more energetically favorable than the experimentally synthesized rhombohedral ($R\bar{3}m$) and hexagonal AlB_2-type MoB_2 ($P6/mmm$) structures.[36] The theoretically calculated strong covalency of the B-Mo bond in the WB_2−MoB_2 structure can provide insight into the observed high solubility of Mo in WB_2 and corresponding high hardness values.

Extrinsic Properties of WB_2−Mo Composites with SiC/B_4C. Once the solubility and Vickers hardness of the WB_2−Mo system were optimized, B_4C and SiC were incorporated as additives to both unsubstituted WB_2 and 30 at% Mo-substituted WB_2 in order to examine the effects of B_4C and SiC precipitation on surface morphology and hardness in multiphase composites. The formation and stability of a phase from liquidus via arc-melting are dependent on the heat of formation as well as the melting point of each respective phase. In general, a phase is more likely to precipitate first upon cooling if it has a higher melting point than another phase and more likely to be stable if it has a highly negative heat of formation.[37] Both carbides have higher melting points than WB_2 (~2450 °C for B_4C[38] and ~2700 °C for SiC[39] versus ~2365 °C for WB_2[40]) and exhibit high thermodynamic stability. As a result, the addition of these secondary phases can be used to template subsequent WB_2 nucleation and grain growth.

Figure 7 shows SEM images of arc-melted samples with increasing SiC content in both WB_2 and $W_{0.70}Mo_{0.30}B_2$ composites. As the amount of elemental Si and C collectively increases in the WB_2 system, the SiC grains increase in size and

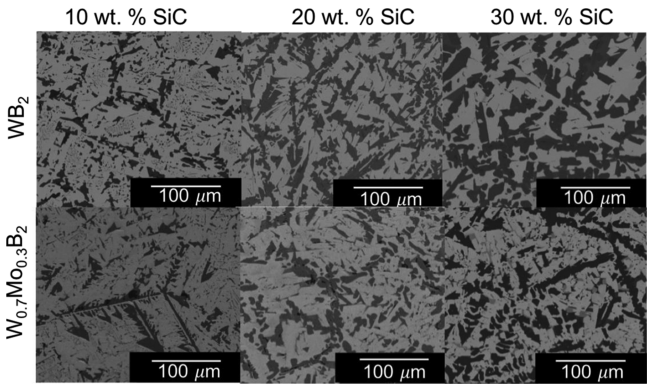

Figure 7. SEM images of (top) WB_2 and (bottom) $W_{0.70}Mo_{0.30}B_2$ with 10, 20, and 30 wt% SiC addition. Light gray regions represent areas of WB_2 and $W_{0.70}Mo_{0.30}B_2$, while dark gray regions represent SiC grains.

density. The addition of SiC to WB_2 led to an overall increase in hardness at 0.49 N from 29.5 ± 1.7 GPa for WB_2 to 45.7 ± 6.6 GPa for WB_2 with 30 wt% SiC (Figure 8a). The reasonably large statistical variation in the measurements may be attributed to variations in grain orientations and the fact that the WB_2 crystal structure is anisotropic. To make sure that this did not bias the data, many different crystallographic orientations were indented. In previous studies from our group, the Vickers hardness of ReB_2 was measured as a function of crystallographic orientation, and statistically significant differences were found in the hardness values measured using indentations parallel to the hexagonal c-axis, compared to those perpendicular to it.[7] Therefore, in this work, the hardness indentation locations were chosen pseudo-randomly to avoid selecting any particular grains. Despite the variation in measured values, the hardness was found to be significantly enhanced relative to pure WB_2 even considering the scatter in the measurements. The hardness value of 45.7 ± 6.6 GPa for WB_2 with 30 wt% SiC is comparable to the hardness achieved in the hardest solid solution, $W_{0.70}Mo_{0.30}B_2$ (45.7 ± 2.5 GPa). SiC has a Vickers hardness range of 21−29 GPa at varying load.[31,41] Therefore, the individual SiC grains do not provide any additional hardening in the WB_2−SiC system. Instead, the SiC precipitates apparently impede the dislocation of smaller WB_2 grains and additional stress must be added for plastic deformation to occur, resulting in a harder bulk material. Interestingly, hardness enhancement occurs only in the unsubstituted WB_2. For the $W_{0.70}Mo_{0.30}B_2$ system, SiC addition resulted in no change in average hardness (Figure 8b). This could be because more dramatic grain structure changes were observed in the pure WB_2 with increasing SiC content, or it may be due to the inherent solid solution hardening and grain boundary strengthening already present in the single-phase $W_{0.70}Mo_{0.30}B_2$ material. These results demonstrate that hardening effects are not necessarily additive, particularly when both intrinsic and extrinsic effects contribute to the overall material properties.

SEM images of WB_2 and $W_{0.70}Mo_{0.30}B_2$ composites with B_4C are shown in Figure 9. Both systems show an increasing grain size and B_4C precipitation as the amount of elemental B and C increases. Unlike SiC, the excess elemental boron added to form the WB_2−B_4C-based composites results in the formation of a WB_4 impurity in addition to B_4C (Figure 10). PXRD data also indicate that less WB_4 is present in $W_{0.70}Mo_{0.30}B_2$

https://doi.org/10.1021/acs.chemmater.2c00386
Chem. Mater. 2022, 34, 5461−5470

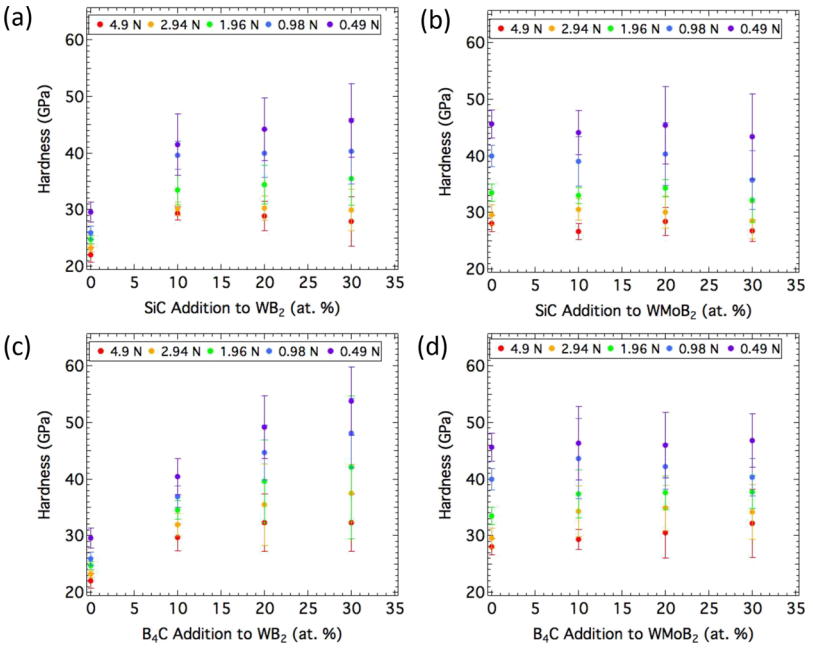

Figure 8. Vickers microindentation hardness versus weight percentage (0−30 wt%) of SiC addition in: (a) WB_2 and (b) $W_{0.70}Mo_{0.30}B_2$ using loads ranging from low (0.49 N) to high (4.9 N). Vickers microindentation hardness versus weight percentage (0−30 wt%) of B_4C addition in: (c) WB_2 and (d) $W_{0.70}Mo_{0.30}B_2$ from low (0.49 N) to high (4.9 N) load.

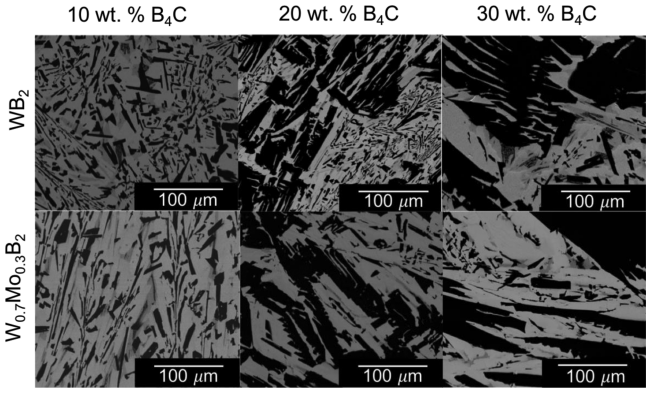

Figure 9. SEM images of (top) WB_2 and (bottom) $W_{0.70}Mo_{0.30}B_2$ with 10, 20, and 30 wt% B_4C additions. Light gray regions represent areas of WB_2 and $W_{0.70}Mo_{0.30}B_2$, while black regions represent B_4C grains. A higher content of additional WB_4 impurity (shown as gray areas surrounding WB_2 and B_4C) occurs in the WB_2 system, where more W is available for tetraboride formation.

composites, where the substitution of Mo results in less W available for WB_4 formation (Figure S5). Similar to the WB_2−SiC composites, increased hardness was observed in the WB_2−B_4C system (Figure 8c). However, the WB_2−B_4C system showed greater hardness enhancement, going from 29.5 ± 1.7 GPa with no B_4C addition to 53.8 ± 6.0 GPa with 30 wt% B_4C addition. This average increase in hardness is due to two additional phases: WB_4 (43.3 ± 2.9 GPa at 0.49 N[42]) and B_4C (~38 GPa[43]), both of which are harder than the parent WB_2 system. In $W_{0.70}Mo_{0.30}B_2$−B_4C, the system again plateaus to a hardness value of approximately 45 GPa at all B_4C percentages (Figure 8d). The fact that the hardness of $W_{0.70}Mo_{0.30}B_2$−B_4C shows no enhancement despite significant grain size changes suggests that grain size is not the primary factor resulting in increased hardness. The explanation more likely lies in the inherent solid solution hardening and grain boundary

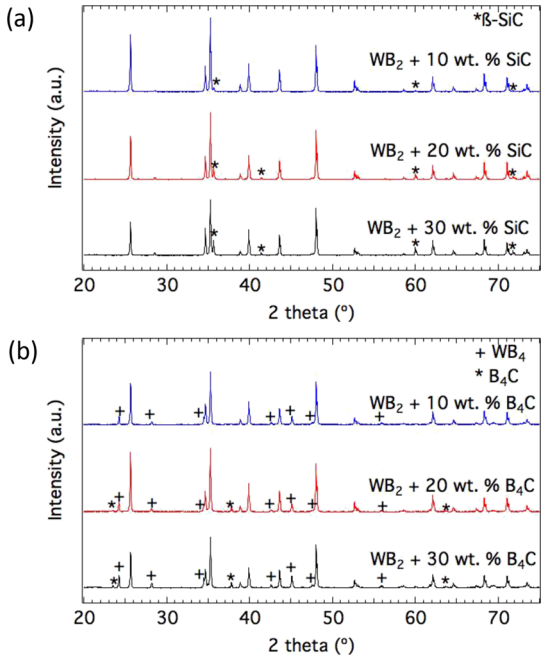

Figure 10. PXRD data of WB_2 with 10, 20, and 30 wt% (a) SiC addition and (b) B_4C. The growth of the secondary β-SiC phase (JCPDS 03-065-0360) is denoted by an asterisk (*) in (a). All patterns show (+) WB_4 (JCPDS 00-019-1373) and (*) B_4C (JCPDS 00-035-0798) in (b).

strengthening already present in the single-phase $W_{0.70}Mo_{0.30}B_2$ material.

Both oxidation resistance and hardness are important factors in cutting tools, where the lifetime and wear resistance of a material greatly affect its performance. To compare the thermal stability of the hardest samples, thermogravimetric studies were performed on fine powders of unsubstituted WB_2 and 30 at% Mo-substituted WB_2 as well as the two hardest

https://doi.org/10.1021/acs.chemmater.2c00386
Chem. Mater. 2022, 34, 5461−5470

composites, WB_2−30 wt% SiC and WB_2−30 wt% B_4C. Figure 11 shows the oxidation behavior of the four samples up to

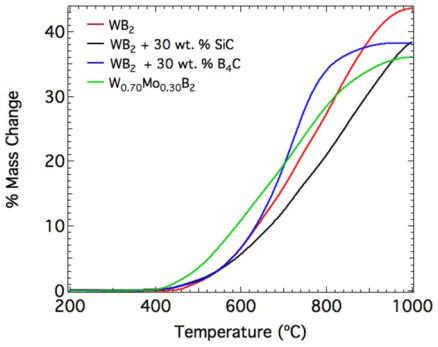

Figure 11. TGA of unsubstituted WB_2 and the three hardest compositions studied in this work.

1000 °C in air. $W_{0.70}Mo_{0.30}B_2$ reaches 10% mass change at the lowest temperature (~580 °C) followed by WB_2−30 wt% B_4C and WB_2 (~640 °C). WB_2−30 wt% SiC does not gain 10% mass until 660 °C. At 700 °C, both $W_{0.70}Mo_{0.30}B_2$ and WB_2−30 wt% B_4C have 20% increased mass, while WB_2 and WB_2−30 wt% SiC do not reach 20% mass change until 740 and 800 °C, respectively. At 30% mass change, the corresponding temperature for WB_2−30 wt% B_4C is 760 °C, much lower than the other three systems. While all systems increase the hardness of unsubstituted WB_2, their effects on oxidation resistance vary. WB_2−30 wt% SiC exhibits the slowest oxidation rate followed by $W_{0.70}Mo_{0.30}B_2$, WB_2 and WB_2−30 wt% B_4C up until 30% mass change. While the composite effect for enhancing oxidation resistance is not fully understood, the presence of SiC and B_4C enhances both hardness and oxidation resistance in the WB_2 system. Understanding the grain morphology, hardness, and thermal stability of these systems provides valuable information toward tailoring boride-based materials for industrial applications.

CONCLUSIONS

The development of materials with high hardness, thermal stability, and cost-effectiveness remains a challenge in the manufacturing and machining industries. In this study, the substitution of 30 at% Mo increased the hardness of the parent WB_2 structure, largely because of intrinsic solid solution effects. These effects are observed both through Vickers hardness measurements and through plateau differential stress values that are both high and remarkably isotropic for a layered crystal structure. Multiphase materials (WB_2 with B_4C and SiC) exhibited additional extrinsic hardening through grain size reduction and phase precipitation. This combination of results indicates that the hardness of WB_2 can be increased both through solid solution effects, which is considered a form of intrinsic hardening, and via composite formation, which is often described as an extrinsic effect. Interestingly, for the WB_2 system, these two mechanisms do not appear to be additive, as the addition of B_4C and SiC to $W_{0.70}Mo_{0.30}B_2$ did not result in increased hardness. These strategies demonstrate the ability to design boride-based materials with enhanced mechanical properties through the microstructure and composition, while using less expensive alloying additives.

ASSOCIATED CONTENT

Supporting Information

The Supporting Information is available free of charge at https://pubs.acs.org/doi/10.1021/acs.chemmater.2c00386.

Tabulated unit cell data and Vickers hardness for $W_{1-x}Mo_xB_2$ (x = 0−0.50); tabulated Vickers hardness and PXRD spectra for WB_2−SiC, $W_{0.70}Mo_{0.30}B_2$−SiC, WB_2−B_4C, and $W_{0.70}Mo_{0.30}B_2$−B_4C; tabulated lattice parameters and volume as a function of pressure; plot of 1-D X-ray diffraction and 2-D cake pattern for $W_{0.70}Mo_{0.30}B_2$; plot of lattice parameters, volume and c/a ratio as a function of pressure; plot of volume change versus pressure for $W_{0.70}Mo_{0.30}B_2$; plot of normalized pressure versus Eulerian strain for $W_{0.70}Mo_{0.30}B_2$; linearized plot of d-spacings as a function of φ angle at highest pressure; plot of d-spacings for selected lattice planes versus pressure (PDF)

AUTHOR INFORMATION

Corresponding Authors

Sarah H. Tolbert − *Department of Chemistry and Biochemistry, Department of Materials Science and Engineering, and California NanoSystems Institute (CNSI), University of California, Los Angeles (UCLA), Los Angeles, California 90095, United States;* orcid.org/0000-0001-9969-1582; Email: tolbert@chem.ucla.edu

Richard B. Kaner − *Department of Chemistry and Biochemistry, Department of Materials Science and Engineering, and California NanoSystems Institute (CNSI), University of California, Los Angeles (UCLA), Los Angeles, California 90095, United States;* orcid.org/0000-0003-0345-4924; Email: kaner@chem.ucla.edu

Authors

Lisa E. Pangilinan − *Department of Chemistry and Biochemistry, University of California, Los Angeles (UCLA), Los Angeles, California 90095, United States;* orcid.org/0000-0002-5507-9989

Shanlin Hu − *Department of Chemistry and Biochemistry, University of California, Los Angeles (UCLA), Los Angeles, California 90095, United States;* orcid.org/0000-0002-2288-499X

Christopher L. Turner − *Department of Chemistry and Biochemistry, University of California, Los Angeles (UCLA), Los Angeles, California 90095, United States*

Jinyuan Yan − *Advanced Light Source, Lawrence Berkeley National Laboratory, Berkeley, California 94720, United States*

Abby Kavner − *Department of Earth, Planetary, and Space Sciences, University of California, Los Angeles (UCLA), Los Angeles, California 90095, United States*

Reza Mohammadi − *Department of Mechanical and Nuclear Engineering, Virginia Commonwealth University, Richmond, Virginia 23284, United States;* orcid.org/0000-0003-4676-4885

Complete contact information is available at: https://pubs.acs.org/10.1021/acs.chemmater.2c00386

Notes

The authors declare the following competing financial interest(s): R.B.K. and C.L.T. have a financial interest in SuperMetalix, Inc.

■ ACKNOWLEDGMENTS

The authors thank M. Kunz and A. MacDowell for technical support at the Lawrence Berkeley National Laboratory (LBNL) beamline 12.2.2. We also thank Professor H.-R. Wenk for equipment support. This work was financially supported by the National Science Foundation Division of Materials Research under grant DMR-2004616 (R.B.K. and S.H.T.). Additional support was provided by the Dr. Myung Ki Hong Endowed Chair in Materials Innovation (R.B.K.), SuperMetalix, Inc.(R.B.K.) and a UCLA Graduate Division Dissertation Year Fellowship (L.E.P.). The startup fund from Virginia Commonwealth University is greatly acknowledged (R.M.). Radial X-ray diffraction experiments were performed at the Advanced Light Source at Laurence Berkeley National Laboratory at Beamline 12.2.2. Beamline 12.2.2 at the Advanced Light Source is a DOE Office of Science User Facility supported under contract no. DE-AC02-05CH11231. This research was partially supported by COMPRES, the Consortium for Materials Properties Research in Earth Sciences under NSF Cooperative Agreement EAR 1606856.

■ REFERENCES

(1) Ezugwu, E. O. Key Improvements in the Machining of Difficult-to-Cut Aerospace Superalloys. *Int. J. Mach. Tools Manuf.* **2005**, *45*, 1353−1367.
(2) Mohammadi, R.; Kaner, R. B. *Superhard Materials*; Scott, R. A. ed.; John Wiley and Sons, Inc., 2012.
(3) Komanduri, R.; Shaw, M. C. Wear of Synthetic Diamond When Grinding Ferrous Metals. *Nature* **1975**, *255*, 211−213.
(4) Westraadt, J. E.; Sigalas, I.; Neethling, J. H. Characterisation of Thermally Degraded Polycrystalline Diamond. *Int. J. Refract. Hard Met.* **2015**, *48*, 286−292.
(5) Kaner, R. B.; Gilman, J. J.; Tolbert, S. H. Designing Superhard Materials. *Science* **2005**, *308*, 1268−1269.
(6) Mansouri Tehrani, A.; Ghadbeigi, L.; Brgoch, J.; Sparks, T. D. Balancing Mechanical Properties and Sustainability in the Search for Superhard Materials. *Integr. Mater. Manuf. Innov.* **2017**, *6*, 1−8.
(7) Chung, H.-Y.; Weinberger, M. B.; Levine, J. B.; Kavner, A.; Yang, J.-M.; Tolbert, S. H.; Kaner, R. B. Synthesis of Ultra-Incompressible Superhard Rhenium Diboride at Ambient Pressure. *Science* **2007**, *316*, 436−439.
(8) Mohammadi, R.; Lech, A. T.; Xie, M.; Weaver, B. E.; Yeung, M. T.; Tolbert, S. H.; Kaner, R. B. Tungsten Tetraboride, an Inexpensive Superhard Material. *Proc. Natl. Acad. Sci. U. S. A.* **2011**, *108*, 10958−10962.
(9) Akopov, G.; Pangilinan, L. E.; Mohammadi, R.; Kaner, R. B. Perspective: Superhard Metal Borides: A Look Forward. *APL Mater.* **2018**, *6*, No. 070901.
(10) Hume-Rothery, W. *Atomic Theory for Students of Metallurgy*, 5th ed.; The Institute of Metals: London, 1969.
(11) Hume-Rothery, W.; Powell, H. M. On the Theory of Super-Lattice Structures in Alloys. *Z. Krist.* **1935**, *91*, 23.
(12) Hume-Rothery, W.; Smallman, R. W.; Haworth, C. W. *The Structure of Metals and Alloys*; The Institute of Metals: London, 1969.
(13) Wu, D.; Zhang, J.; Huang, J. C.; Bei, H.; Nieh, T. G. Grain-Boundary Strengthening in Nanocrystalline Chromium and the Hall−Petch Coefficient of Body-Centered Cubic Metals. *Scr. Mater.* **2013**, *68*, 118−121.
(14) Akopov, G.; Yeung, M. T.; Turner, C. L.; Mohammadi, R.; Kaner, R. B. Extrinsic Hardening of Superhard Tungsten Tetraboride Alloys with Group 4 Transition Metals. *J. Am. Chem. Soc.* **2016**, *138*, 5714−5721.
(15) Nagamatsu, J.; Nakagawa, N.; Muranaka, T.; Zenitani, Y.; Akimitsu, J. Superconductivity at 39K in Magnesium Diboride. *Nature* **2001**, *410*, 63−64.
(16) Park, H.; Encinas, A.; Scheifers, J. P.; Zhang, Y.; Fokwa, B. P. T. T. Boron-Dependency of Molybdenum Boride Electrocatalysts for the Hydrogen Evolution Reaction. *Angew. Chem., Int. Ed.* **2017**, *56*, 5575−5578.
(17) Lech, A. T.; Turner, C. L.; Lei, J.; Mohammadi, R.; Tolbert, S. H.; Kaner, R. B. Superhard Rhenium/Tungsten Diboride Solid Solutions. *J. Am. Chem. Soc.* **2016**, *138*, 14398−14408.
(18) Park, H.; Zhang, Y.; Lee, E.; Shankhari, P.; Fokwa, B. P. T. High-Current-Density HER Electrocatalysts: Graphene-like Boron Layer and Tungsten as Key Ingredients in Metal Diborides. *ChemSusChem* **2019**, *12*, 3726−3731.
(19) Burdett, J. K.; Canadell, E.; Miller, G. J. Electronic Structure of Transition-Metal Borides with the AlB2 Structure. *J. Am. Chem. Soc.* **1986**, *108*, 6561−6568.
(20) Aronsson, B.; Lundström, T.; Engström, I. Some Aspects of the Crystal Chemistry of Borides, Boro-Carbides and Silicides of the Transition Metals. In *Anisotropy in Single-Crystal Refractory Compounds: Proceedings of an International Symposium on Anisotropy in Single-Crystal Refractory Compounds, held on June 13--15, 1967, in Dayton Ohio. Sponsored by the Ceramics and Branch of the air Force Materials L*; Vahldiek, F. W., Mersol, S. A., Eds.; Springer US: Boston, 1968; pp 3−22.
(21) La Placa, S. J.; Post, B. The Crystal Structure of Rhenium Diboride. *Acta Crystallogr.* **1962**, *15*, 97−99.
(22) Frotscher, M.; Hölzel, M.; Albert, B. Crystal Structures of the Metal Diborides ReB_2, RuB_2, and OsB_2 from Neutron Powder Diffraction. *Zeitschrift fur Anorg. und Allg. Chemie* **2010**, *636*, 1783−1786.
(23) Lundström, T. The Structure of Ru_2B_3 and $WB_{2.0}$ as Etermined by Single-Crystal Diffractometry, and Some Notes on the W-B System. *Ark. Kemi* **1968**, *30*, 115−127.
(24) Frotscher, M.; Klein, W.; Bauer, J.; Fang, C.-M.; Halet, J.-F.; Senyshyn, A.; Baehtz, C.; Albert, B. M_2B_5 or M_2B_4? A Reinvestigation of the Mo/B and W/B System. *Zeitschrift für Anorg. und Allg. Chemie* **2007**, *633*, 2626−2630.
(25) Pangilinan, L. E.; Turner, C. L.; Akopov, G.; Anderson, M.; Mohammadi, R.; Kaner, R. B. Superhard Tungsten Diboride-Based Solid Solutions. *Inorg. Chem.* **2018**, *57*, 15305−15313.
(26) Zhao, F.; Qiu, L.; Ding, Z.; Li, Y.; Yao, B.; Shen, W.; Li, Q.; Zhu, P. Synthesis and Characterization of WB_2-WB_3-B_4C Hard Composites. *Int. J. Refract. Hard Met.* **2019**, *82*, 268−272.
(27) Neuman, E. W.; Brown-Shaklee, H. J.; Hilmas, G. E.; Fahrenholtz, W. G. Titanium Diboride-Silicon Carbide-Boron Carbide Ceramics with Super-High Hardness and Strength. *J. Am. Ceram. Soc.* **2018**, *101*, 497−501.
(28) Asl, M. S.; Kakroudi, M. G.; Noori, S. Hardness and Toughness of Hot Pressed ZrB2−SiC Composites Consolidated under Relatively Low Pressure. *J. Alloys Compd.* **2015**, *619*, 481−487.
(29) Slater, J. C. Atomic Radii in Crystals. *J. Chem. Phys.* **1964**, *41*, 3199−3204.
(30) Toby, B. H.; Von Dreele, R. B. *GSAS-II*: The Genesis of a Modern Open-Source All Purpose Crystallography Software Package. *J. Appl. Crystallogr.* **2013**, *46*, 544−549.
(31) Quinn, J. B.; Quinn, G. D. Indentation Brittleness of Ceramics: A Fresh Approach. *J. Mater. Sci.* **1997**, *32*, 4331−4346.
(32) Ivankov, A. A. *Handbook of Hardness Data*; Naukova Dumka: Kiev, 1968.
(33) Lei, J.; Hu, S.; Turner, C. L.; Zeng, K.; Yeung, M. T.; Yan, J.; Kaner, R. B.; Tolbert, S. H. Synthesis and High-Pressure Mechanical Properties of Superhard Rhenium/Tungsten Diboride Nanocrystals. *ACS Nano* **2019**, *13*, 10036−10048.
(34) Xie, M.; Mohammadi, R.; Mao, Z.; Armentrout, M. M.; Kavner, A.; Kaner, R. B.; Tolbert, S. H. Exploring the High-Pressure Behavior of Superhard Tungsten Tetraboride. *Phys. Rev. B: Condens. Matter Mater. Phys.* **2012**, *85*, 1−8.
(35) Xie, M.; Mohammadi, R.; Turner, C. L.; Kaner, R. B.; Kavner, A.; Tolbert, S. H. Exploring Hardness Enhancement in Superhard Tungsten Tetraboride-Based Solid Solutions Using Radial X-Ray Diffraction. *Appl. Phys. Lett.* **2015**, *107*, No. 041903.

https://doi.org/10.1021/acs.chemmater.2c00386
Chem. Mater. 2022, 34, 5461−5470

(36) Ding, L.-P.; Shao, P.; Zhang, F.-H.; Lu, C.; Ding, L.; Ning, S. Y.; Huang, X. F. Crystal Structures, Stabilities, Electronic Properties, and Hardness of MoB_2: First-Principles Calculations. *Inorg. Chem.* **2016**, *55*, 7033−7040.
(37) Niessen, A. K.; De Boer, F. R. The Enthalpy of Formation of Solid Borides, Carbides, Nitrides, Silicides and Phosphides of Transition and Noble Metals. *J. Less Common Met.* **1981**, *82*, 75−80.
(38) Morosin, B.; Aselage, T. L.; Feigelson, R. S. Crystal Structure Refinements of Rhombohedral Symmetry Materials Containing Boron-Rich Icosahedra. *MRS Proc.* **1987**, *97*, 145.
(39) Wright, W. V. J.; Bartels, F. T. C. Considerations of the Ternary System Carbon-Silicon-Germanium. In *Proceedings of the Conference on Silicon Carbide*; O'Connor, J. R., Smiltens, J., Eds.; Pergamon Press: New York, 1960; pp 31−36.
(40) Duschanek, H.; Rogl, P.; Duschanek, H.; Rogl, P.; Duschanek, H.; Rogl, P.; Duschanek, H.; Rogl, P. Critical Assessment and Thermodynamic Calculation of the Binary System Boron-Tungsten (B-W). *J. Phase Equilibria* **1995**, *16*, 150−161.
(41) Brazhkin, V. V.; Lyapin, A. G.; Hemley, R. J. Harder than Diamond: Dreams and Reality. *Philos. Mag. A* **2002**, *82*, 231−253.
(42) Mohammadi, R.; Xie, M.; Lech, A. T.; Turner, C. L.; Kavner, A.; Tolbert, S. H.; Kaner, R. B. Toward Inexpensive Superhard Materials: Tungsten Tetraboride-Based Solid Solutions. *J. Am. Chem. Soc.* **2012**, *134*, 20660−20668.
(43) Crouch, I. G.; Franks, G. V.; Tallon, C.; Thomas, S.; Naebe, M. Glasses and Ceramics. In *The Science of Armour Materials*; Elsevier, 2017; pp 331−393.

https://doi.org/10.1021/acs.chemmater.2c00386
Chem. Mater. 2022, 34, 5461−5470